Design and fabrication of blazed gratings for a waveguide-type head mounted display

MARIE-ALINE MATTELIN [1,*], ANA RADOSAVLJEVIC [1], JEROEN MISSINNE [1], DIETER CUYPERS [1], GEERT VAN STEENBERGE [1]

[1] *Center for Microsystems Technology (CMST), Ghent University and imec, 9052 Ghent, Belgium*
[*] *mariealine.mattelin@ugent.be*

Abstract: In a waveguide-type display for augmented reality, the image is injected in the waveguide and extracted in front of the eye appearing superimposed on the real world scene. An elegant and compact way of coupling these images in and out is by using blazed gratings, which can achieve high diffraction efficiencies. We report the design of blazed gratings for green light (λ = 543 nm) and a diffraction angle of 43°. The blazed gratings with a pitch of 508 nm and a fill factor of 0.66 are fabricated using grayscale electron beam lithography. We outline the subsequent replication in a polymer waveguide material with ultraviolet nanoimprint lithography and confirm a throughput efficiency of 17.4%. We finally show the in- and outcoupling of an image through two blazed gratings appearing sharp and non-distorted in the environment.

1. Introduction

With the virtual reality (VR) and augmented reality (AR) application's boom, head-mounted displays (HMDs) are gaining a lot of attention. The waveguide approach is of particular interest because the HMD can be made small and light-weighted [1–4]. The general principle of a waveguide-type HMD is schematically displayed in Fig. 1. Various waveguide based techniques are used in modern HMDs such as reflective optics, polarized optics, diffraction optics and holographic optics. These are briefly discussed below [5].

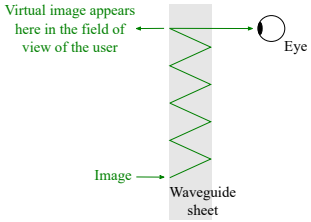

Fig. 1. Schematic representation of a waveguide-type HMD.

In Google Glass and Epson's Moverio the image is projected on a semi-reflective mirror in front of the user's eye without any loss or degradation, so the system has a high optical efficiency and can be provided at a low cost. The main drawback is the field of view (FOV), which is proportional to the size of the reflector and the waveguide thickness. Thicker waveguides are less practical to integrate, e.g. in glasses, and they also affect the image quality: when traveling through a thick waveguide the image can be observed as highly distorted.

Polarized waveguides, on the other hand, make use of total internal reflection (TIR) on a partially reflective polarized surface where selected light waves cancel out exciting into the viewer's eye. The polarized waveguides offer a large field of view, but a low optical efficiency at a high cost as they require multiple layers of coatings and polarized reflectors which should be parallelized and polished to guide the light waves. Lumus DK-50 AR glasses are based on this

approach.

Other possibilities are the use of holographic or diffractive optical elements (HOEs and DOEs). Here, the light is coupled in a waveguide under a certain angle and coupled out in front of the eye after propagating in the waveguide by TIR. As such, a virtual image or information can be displayed on the real world scene without impairing the view of the outside scene. HOEs are used by Sony's Smart Eyeglass Display and DOEs by Vuzix and Microsoft's HoloLens. The concept of HOEs and DOEs is similar, but their fabrication method is not. HOEs are fabricated with holographic imaging processes whereby changes are made in bulk material. This is typically done by recording the interference pattern of 2 light beams in a photosensitive material. HOEs can achieve high optical efficiencies, but fabrication is complex and less scalable, in contrast to DOEs. DOEs are realized as corrugations at the surface and can be replicated by making a copy through for example an imprinting process. The standard symmetric DOEs are easy to fabricate and allow mass production, but for normal incidence their efficiency is low. In [6] binary surface relief gratings are designed to achieve efficiencies of 70-80%. These binary gratings have grating periods larger than one wavelength and use subwavelength structures within each period in order to achieve high efficiencies. However, such gratings would be very challenging to fabricate and replicate as they are extremely small and have a very high aspect ratio. In this paper we want to investigate the possibilities of high efficient asymmetric DOEs, such as slanted or blazed gratings, whose fabrication processes are scalable to mass production.

For slanted grating fabrication the sample should be mounted on a slanted holder so that slots can be etched under an angle with, for example, focused ion beam (FIB) under an iodine atmosphere [7] or by means of chemically assisted or refractive ion beam etching [8, 9]. The fabrication of slanted gratings requires specialized equipment, hence we focus on blazed gratings. Blazed gratings can be fabricated with either mechanical ruling, grayscale electron-beam lithography or holographic lithography combined with ion milling or anisotropic etching. During a mechanical ruling process the triangular groove profile must be accurately controlled across the entire surface of the grating. The process condition, in particular, the ruling tool wear, has to be constantly monitored and compensated to ensure a tight control of the ruled groove profile. These high standard specifics required by the gratings demand a high degree of precision. As a result, only a few facilities in the world are able to mechanically rule the master gratings [10]. Holographic lithography, on the other hand, is mostly used for symmetric structures and should be combined with ion milling [11] or anisotropic KOH etching [12] to achieve asymmetric structures. As these combined processes are expensive and time consuming, we focus on grayscale electron beam lithography in this paper. Blazed gratings can be fabricated by the combination of grayscale electron-beam lithography (EBL) and thermal reflow. Using grayscale EBL multilevel structures are fabricated which are reflowed into continuous slopes by thermally activated selective topography equilibration (TASTE) [13] to achieve rounded and blazed structures [14, 15]. We choose a fabrication flow using grayscale EBL without thermal reflow [16] as we want to limit the process steps to achieve a well-controlled fabrication flow.

To integrate the blazed gratings in a waveguide-type HMD, a suitable replication process is needed to copy the grating structures from a master mold to a waveguide sheet. Polymers offer the possibility of replicating gratings by imprinting with a potentially high cost efficiency. A stamp-based imprinting process allows the definition of nanostructures with very good control over the dimensions and the profile of the printed features [17, 18]. In [19] the use of ultraviolet nanoimprint lithography (UV-NIL) is reported for replicating a 3D pyramid-shaped array. This process is also chosen here because it can be scaled to roll-to-roll or roll-to-plate high-throughput manufacturing [20, 21].

We design blazed gratings with a pitch of 508 nm and an in- and outcoupling efficiency of more than 60% and completely describe the process of the optimization of grayscale EBL to achieve these blazed grating profiles. We outline the replication of the 3D grating structures

using UV-NIL on a waveguide sheet to demonstrate the HMD principle with blazed gratings. We show that an image injected in the waveguide and extracted in front of the eye appears sharp and non-distorted superimposed on the real world scene.

2. Blazed grating design

Figure 2 shows the optical design layout of an HMD consisting of a waveguide for image transmission, surface relief gratings for in- and outcoupling of an image to the waveguide and an optical engine used to generate the image which is transmitted through the waveguide. A lens is added to collimate the image before incoupling. The waveguide material is PMMA (poly methyl methylacrelate), with a 30 μm-thick OrmoCore layer (Microresist Technology, Berlin, Germany) on top of which the gratings are imprinted.

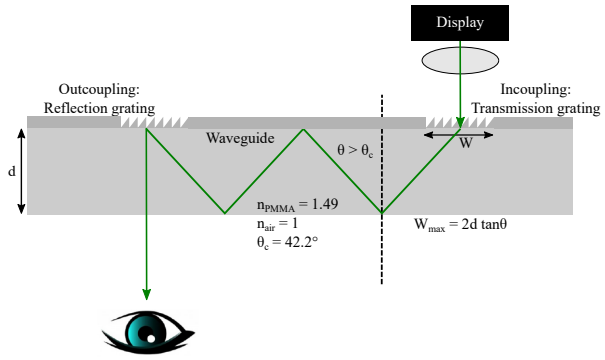

Fig. 2. Optical design layout of a waveguide-type HMD with gratings.

Both gratings are imprinted on the same side of the waveguide sheet for easier fabrication. For practical reasons, the light engine is also on this side. Hence, the incoupling grating should work as a transmission grating, while the outcoupling grating should be a reflection grating. Light propagates between the in- and outcoupling gratings in the waveguide due to TIR at the polymer/air interfaces. The transmission incoupling grating should diffract most of the energy of the normally incident light from the light source to the first diffraction order $m = -1$. This first diffraction order must be larger than the critical angle for TIR, as is shown in Fig. 3(a). At the outcoupling grating, most of the energy of the light coming under an angle should be reflected towards the eye to the zeroth order, this is illustrated in Fig. 3(b).

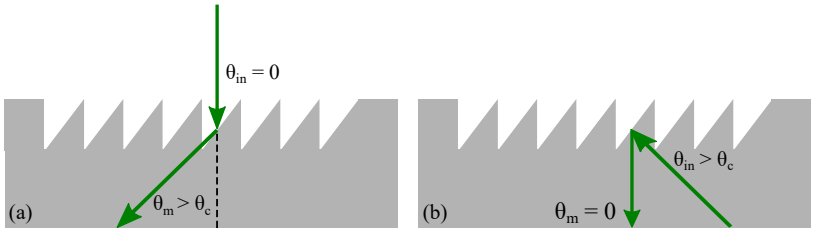

Fig. 3. Schematic representation of the (a) input transmission and (b) output reflection blazed gratings. The green arrows show the light path.

Under normal light conditions, human eyes are most sensitive to a yellowish-green color [22]. Therefore, green light (λ = 543 nm) is used for projecting the images. At this wavelength, the refractive indices of PMMA and OrmoCore are, respectively, 1.49 and 1.565 and the minimal angle for TIR at the PMMA/air interface is 42.2°. To avoid backcoupling of incoupled light,

the maximal length of the incoupling grating is $W_{max} = 2d\ tan\theta$, where d is the waveguide thickness and θ is the diffraction angle. For a diffraction angle of 43° and a waveguide thickness of 5 mm, images of maximum 9.3 mm broad can be launched ($W_{max} = 9.3\ mm$).

The diffraction angle depends both on the wavelength of the incoupled light and on the grating period and is defined by the grating equation. The efficiency of the gratings with a fixed period depends on the profile of the grating and can be calculated numerically. Therefor we use the finite difference time domain (FDTD) method, implemented in the commercially available FDTD software (Lumerical Inc., Vancouver, BC, Canada). The grating length of 5 mm is impractical to be directly applied in simulation. Hence, only one grating period is simulated and periodic boundary conditions are applied. These boundary conditions imply that the grating length is infinite. We can state that this is a valid assumption in our case as the number of periods in a 5 mm long grating is very large. In the vertical direction the simulation window is 4 μm high, so the simulation only runs in the 30 μm-thick OrmoCore layer and does not take the substrate into account. In Fig. 4 the grating period and the number of periods in a 5 mm long first order diffraction grating in OrmoCore are shown as a function of the diffraction angle for a wavelength of 543 nm. For a diffraction angle of 43° the grating period is 508 nm.

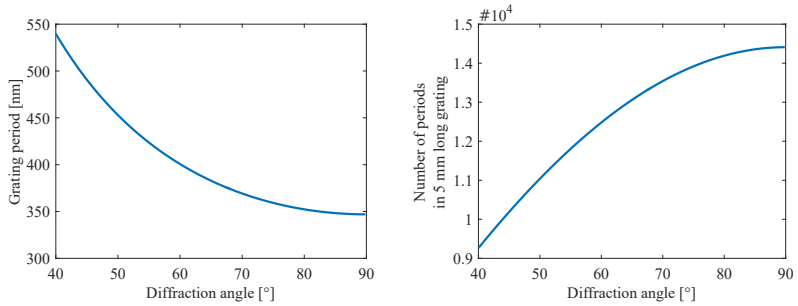

Fig. 4. The grating period and the number of periods in a 5 mm long first order diffraction grating in OrmoCore as a function of the diffraction angle for a wavelength of 543 nm.

In Fig. 5(a) the transmitted power to the first diffraction order at 43° is shown as a function of the grating height H and fill factor FF for a blazed grating in OrmoCore. The results are obtained for light polarized parallel to the grating lines. The grating period is 508 nm. For a grating height of 700 nm and a fill factor of 1, a maximal efficiency of 65% can be reached. However, such gratings might be difficult to fabricate with EBL due to the large aspect ratio and the proximity effect which affects the grating shape when the grating teeth are close to each other. On the other hand, there is, next to this maximum, a broad range of parameters for which more than 60% efficiency can be achieved.

Figure 5(b) shows the efficiency of the output reflection grating as a function of the grating height and fill factor for a blazed grating in OrmoCore. A maximal efficiency of 64.56% can be obtained for a grating height of 390 nm and a fill factor of 0.58. Designing transmission and reflection gratings for larger diffraction angles (> 45°) results in lower grating efficiencies.

Next to triangular blazed gratings, also two other grating shapes are evaluated using Lumerical. Since we do not reflow the e-beam structures, the grating profile can deviate from a smooth triangular shape although the EBL parameters are carefully optimized to suppress deviations as much as possible. During the fabrication it was noticed that the gratings tend to have a trapezoidal shape or a triangular shape with an extra top. So, these profiles are also simulated to confirm that a slightly different shape does not affect the efficiency a lot. First, a trapezoidal grating shape as shown in Fig. 6 is investigated. Here, Δ is the grating period, W is the width of the trapezoidal

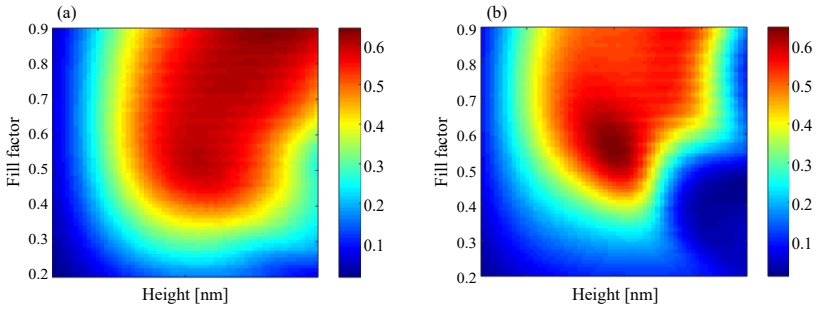

Fig. 5. Efficiency of blazed gratings: (a) Input transmission grating: efficiency of power transmission to the first diffraction order. (b) Output reflection grating: efficiency of power reflection to the zeroth diffraction order.

grating bottom base which is defined as $W = FF * \Delta$ and W_1 is the width of the trapezoidal grating top base which is defined as $W_1 = \eta W$.

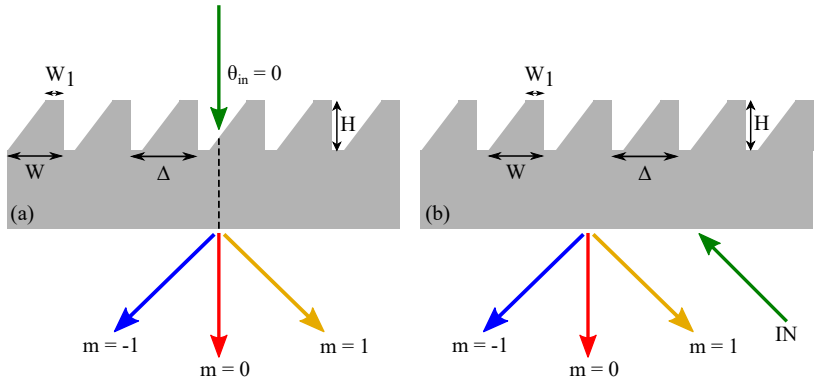

Fig. 6. Schematic representation of the (a) input transmission (b) output reflection trapezoidal gratings. Each color represents another diffraction order.

Figure 7(a) shows the efficiency to the zeroth and first diffraction orders of a trapezoidal input transmission grating in OrmoCore as a function of η. The grating period Δ, fill factor FF and height H are fixed to 508 nm, 0.58 and 390 nm, respectively. The value $\eta = 0$ corresponds to a triangular grating profile while $\eta = 1$ corresponds to a binary grating. Increasing the value of η decreases the amount of light coupled to the first diffraction order $m = -1$ while the amount of light coupled to the zeroth $m = 0$ and first order $m = 1$ diffraction increases. In case of a symmetric binary grating ($\eta = 1$), most of the light is transmitted to the zeroth order and the efficiencies of diffraction in the $\pm$ 1 order become equal. Figure 7(b) displays the diffraction order efficiencies of a trapezoidal output reflection grating in OrmoCore as a function of η for the same values of the grating period, fill factor and height. A drop in efficiency to the zeroth order $m = 0$ for $\eta > 0.32$ can be noticed.

Second, a triangular shape with top, as shown in Fig. 8, is examined where Δ is the pitch, H is the total height and D is the total width, defined as $D = FF * \Delta$. The top is characterized by H_1: the height of the grating without the top, and D_{top}: the width of the grating top which is defined in $\psi = \frac{D - D_{top}}{D}$.

The efficiencies of such in- and outcoupling gratings in OrmoCore as a function of the two parameters H_1 and ψ are simulated for a grating pitch Δ, grating height H and width D of 508

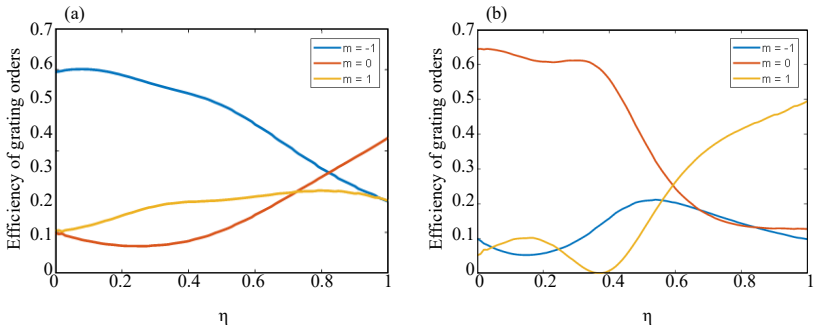

Fig. 7. Efficiency of trapezoidal gratings to the zeroth and first diffraction orders: (a) Input transmission grating (b) Output reflection grating.

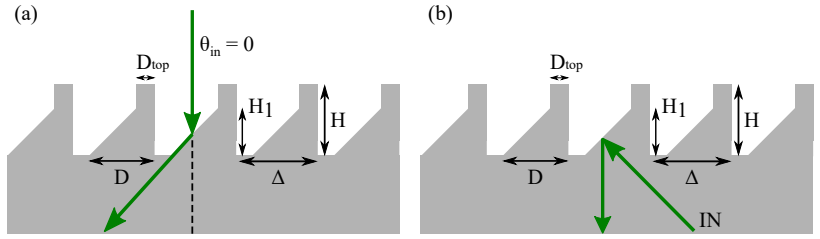

Fig. 8. Schematic representation of the (a) input transmission (b) output reflection blazed gratings with top.

nm, 480 nm and 300 nm, respectively, and are shown in Fig. 9. Also in these graphs there is a broad range of parameters corresponding to a grating with an efficiency of more than 55%.

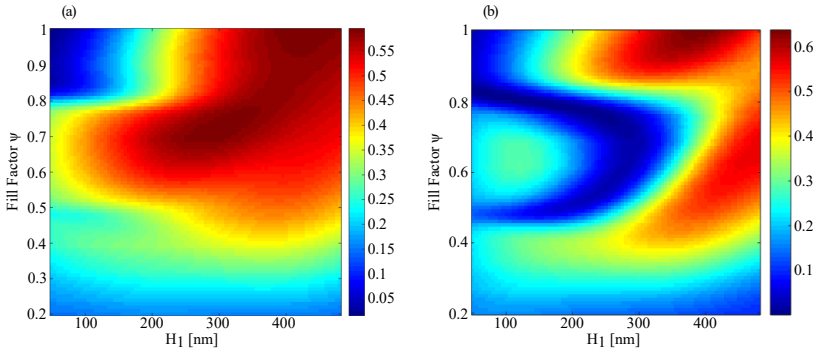

Fig. 9. Efficiency of blazed gratings with top: (a) Input transmission grating: efficiency of power transmission to the first diffraction order. (b) Output reflection grating: efficiency of power reflection to the zeroth diffraction order.

As a comparison, the efficiency of a binary grating in OrmoCore is simulated as well. For a binary grating with a pitch, fill factor and height of 508 nm, 0.5 and 190 nm, respectively, an incoupling efficiency of 30% and an outcoupling efficiency of 18% are simulated.

3. Fabrication methods

To realize a waveguide-type HMD with blazed gratings, first a master mold with two blazed gratings is realized using grayscale EBL which is then replicated onto a waveguide sheet using

UV-NIL. EBL allows 3D patterning by using dose-modulated exposure and wet development. To realize the triangular grating profile different grating lines are exposed with a different dose in a sensitive and high-contrast EBL resist. For the replication of the master mold two replication steps are involved, as is shown in Fig. 12. In the first imprint step the inverse shape of the master mold is replicated into a soft mold. In the second step the soft mold is rolled over the polymer material to realize the grating structures on the waveguide substrate.

3.1. Master fabrication using grayscale electron-beam lithography

3.1.1. Material choice

The core of our fabrication technology for the master grating is the EBL process. The system used is a Raith Voyager EBL machine (Raith Nanofabrication, Dortmund, Germany) with a voltage acceleration of 50 keV. First, a suited resist-developer system has to be selected. The primary characterization factors when choosing this are contrast and sensitivity. Contrast is the ability of a resist to differentiate between exposed and unexposed areas, while sensitivity defines the variation of the resist height with the exposure dose. Together, these two parameters determine the contrast curve of a resist which is a plot of the remaining resist thickness after development as a function of the e-beam dose [23]. The higher the dose, the lower is the molecular weight due to chain scission. Consequently, the development rate in a certain developer is higher for larger doses [15]. Two positive resists, 950 PMMA (poly methyl methylacrelate) A7 (MicroChem, Westborough, MA, USA) and ARP 6200.13 (Allresist, Strausberg, Germany) are investigated. The resists are spin coated on an air plasma cleaned (Diener Pico, 190 W 40 kHz generator, 24 s, 0.8 mbar; Diener electronic, Ebhausen, Germany) Si substrate and baked on a hotplate. 6 μm wide lines are exposed with a dose variation ranging from 0 to 450 $\frac{\mu C}{cm^2}$ to determine the dose-depth correlation. The development is done in MIBK:IPA and n-amyl acetate for the PMMA- and ARP-resist samples, respectively. Afterwards, they are rinsed in IPA to stop the development and blown dry by nitrogen. In Fig. 10 the resulting contrast curves are plotted. In the contrast curve, the sensitivity of the resist-developer system is the dose D_{100} at which the resist is completely developed. The contrast γ is the slope of the curve and is given by the following equation [Eq. (1)]:

$$\gamma^{-1} = log_{10}\frac{D_{100}}{D_0} \tag{1}$$

D_0 is the highest dose at which the resist is not yet affected by electron irradiation [23]. The experimental values for the contrast γ and the sensitivity D_{100} for the resist-developer systems investigated here are listed in table 1.

Contrast γ and sensitivity D_{100} decrease for a longer developer time for the same resist-developer system. ARP has a higher sensitivity than PMMA, this minimizes the writing time, but this also implies that the window over which the dose can be varied is smaller. In the system (950 PMMA A7 - MIBK:IPA 1:3 20 s), with a sensitivity of 440 $\frac{\mu C}{cm^2}$ and in the system (950 PMMA A7 - MIBK:IPA 1:3 40 s) with a sensitivity of 350 $\frac{\mu C}{cm^2}$, more than 25 dose levels can be used for grayscale EBL. These medium contrast resist-developer systems are chosen as a higher contrast system requires a more accurate dose control and gives no further benefit [15].

3.1.2. Master fabrication

Following the previous discussion the 950 PMMA A7 - MIBK:IPA 1:3 20-40 s resist-developer systems are chosen to fabricate the master mold with blazed gratings. A 4" Si wafer is treated with plasma (Diener Pico, 190 W 40 kHz generator, 24 s, 0.8 mbar, gas used: air) and spin coated with 950 PMMA A7 (1500 rpm, 45 s, coating thickness = 850 nm). A soft baking step is applied (150°C, 90 s) before AR-PC 5090 (Allresist, Strausberg, Germany), a conductive protective coating, is spin coated (2000 rpm, 60 s, coating thickness = 60 nm) and soft baked

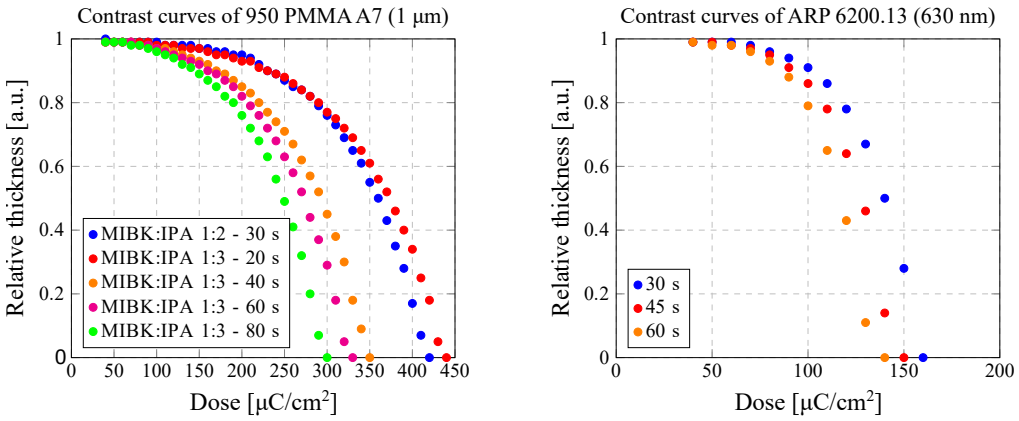

Fig. 10. Contrast curves for 950 PMMA A7 and ARP 6200.13 with different developer solutions and times.

Table 1. Contrast γ and sensitivity D_{100} for different resist-developer systems.

Resist	Developer	γ	D_{100} [$\frac{\mu C}{cm^2}$]
PMMA	MIBK:IPA 1:2 30 s	7.07	420
PMMA	MIBK:IPA 1:3 20 s	6.85	440
PMMA	MIBK:IPA 1:3 40 s	6.50	350
PMMA	MIBK:IPA 1:3 60 s	5.55	330
PMMA	MIBK:IPA 1:3 80 s	2.14	300
ARP	n-amyl acetate 30 s	8.19	160
ARP	n-amyl acetate 45 s	5.54	150
ARP	n-amyl acetate 60 s	4.91	140

(90°C, 120 s). The resist is exposed in a Raith Voyager EBL system with a voltage acceleration of 50 keV. A small beam current of 0.41-0.5 nA is selected to improve the resolution. A grating of several mm^2 is exposed by stitching multiple writefields of 200x500 μm^2. Within one writefield it is the electron-beam which scans the area to be exposed, ensuring a very good control over the patterning. Between different writefields it is the stage which moves, eventually leading to stitching errors. Several accurate alignment procedures before the exposure can minimize these errors. One writefield is scanned in multiple passes; in each pass a grating is exposed with the same pitch but with a different fill factor and dose. This is schematically shown in Fig 11. A different dose results in a different resist thickness after development according to the corresponding contrast curves in Fig. 10. After the exposure, the wafer is rinsed with DI water to remove the conductive coating, developed in MIBK:IPA 1:3 for 20-40 s, rinsed in IPA and blown dry with a nitrogen gun. Cross section inspection of the grating profile is done with a focused ion beam (FIB) scanning electron microscope (SEM) and reveals the desired relief structure. Multiple cycles of EBL and cross section inspection were needed to optimize the e-beam writing parameters, electron-dose distributions and fill factors of the different grating layers.

To evaluate and compare the blazed gratings to binary gratings, a master with two 5x5 mm^2 binary gratings is fabricated. Therefor AZ nLOF 2070 (MicroChemicals, Ulm, Germany) [24] is chosen as an e-beam resist. Before spin coating, this resist is diluted with AZ EBR 70/30 (AZ

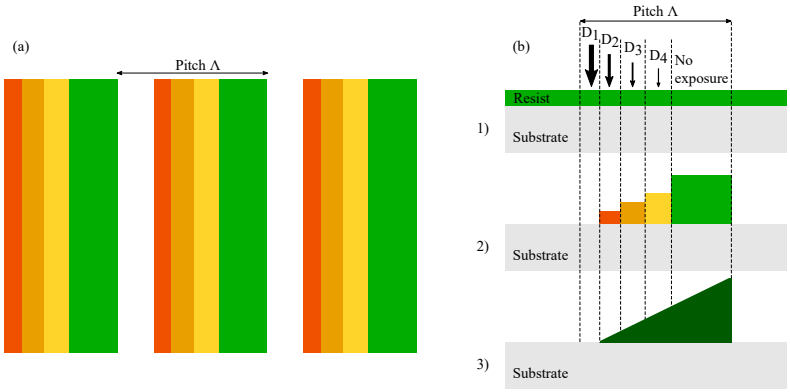

Fig. 11. Schematic overview of the e-beam exposure strategy with multiple grating layers. Each grating layer is exposed with a different dose: D_1 being the highest and D_4 being the lowest, between D_4 from one grating period and D_1 from the next grating period there is an unexposed region. (a) Shows the top view of a grating with different layers, (b) shows the side view: 1) dose-modulated exposure 2) estimation of the remaining resist thickness according to the contrast curve 3) actual grating profile.

nLOF: AZ EBR 1:2). A plasma treated 4" Si wafer is spin coated with diluted AZ nLOF 2070 (5000 rpm, 30 s, coating thickness = 400 nm) and soft baked (100°C, 60 s). The resist is exposed in the Raith Voyager EBL system with a voltage acceleration of 50 keV, a beam current of 0.47 nA and a dose of 45 $\frac{\mu C}{cm^2}$. After the exposure, the sample is baked (110°, 120 s), developed in AZ 826 MIF for 45 s, rinsed in DI and blown dry with a nitrogen gun. To achieve a depth of 190 nm, as was simulated, the gratings are etched in Si using refractive ion etching (Advanced Vacuum's Vision 320 RIE, Plasma-Therm, St. Petersburg, FL, USA).

3.2. Replication of the gratings on waveguides using UV-NIL

The transfer of the blazed and binary gratings on the master mold to the final waveguide sheet is done using two UV-NIL steps and is schematically shown in Fig. 12. First, a soft stamp is fabricated by replicating the master mold into a UV-curable transparent perfluoropolyether (PFPE) polymer. This polymer is prepared by adding 3% photoinitiator to working stamp material EVGNIL UV/AF1 (EV Group, St.Florian am Inn, Austria) by weight. After manually mixing thoroughly, the viscous mixture is let to rest for 60 min for degassing. Subsequently, the mixture is spin coated at a slow speed (500 rpm, 60 s) to achieve a relatively thick but homogeneous layer on the master mold. The material is covered with a PET foil and the stack is UV exposed (30 $\frac{mW}{cm^2}$, 60 s). Afterwards, the stack is peeled off and the structures are reverse copied in the PFPE material. This soft stamp is now used for imprinting the structures in the final polymer material on the waveguide substrate. OrmoCore (Microresist Technology, Berlin, Germany) is spin coated on a clean and plasma treated (Diener Pico, 190 W 40 kHz generator, 24 s, 0.8 mbar, gas used: air) PMMA substrate (3000 rpm, 30 s, coating thickness = 30 μm). The soft stamp is brought in contact with the OrmoCore coating in a rolling motion to avoid air being trapped. This stack is UV exposed (30 $\frac{mW}{cm^2}$, 60 s) after which the soft stamp is manually peeled off.

4. Results and discussion

4.1. The blazed grating profile

To investigate the blazed grating profiles, cross sections are made with FIB SEM (Nova 600 NanoLab, FEI Company, Hillsboro, OR, USA). To avoid charging in the FIB SEM, the preparation

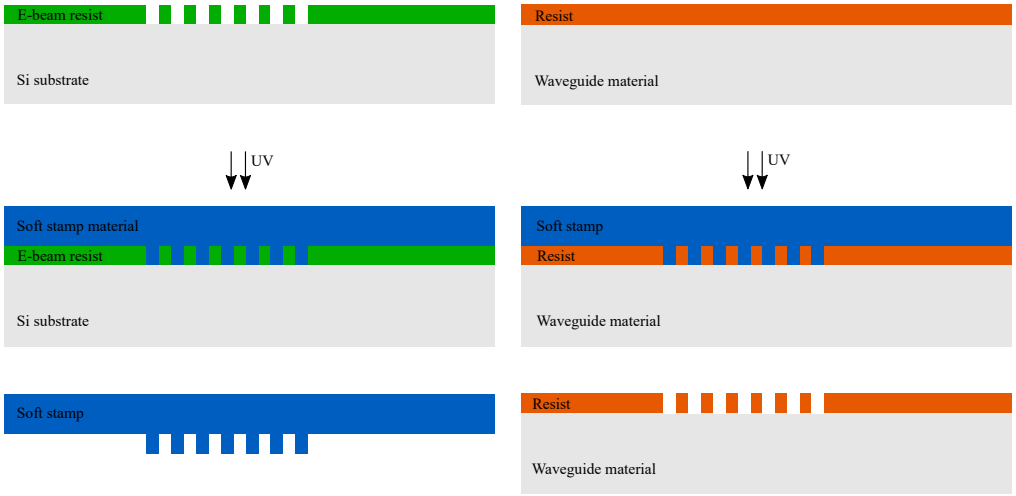

Fig. 12. Schematic overview of the two-step imprinting process.

is started with the sputtering of a gold layer of 10-15 nm (SPI Module Sputter Coater, Structure Probe Inc., West Chester, PA, USA). Then, two layers of platinum (Pt) are deposited, one with the electron-beam and one with the ion beam, to protect the structures from further processing. The actual cross sectioning is done in two steps: a rough milling step is followed by a cleaning step.

In Fig. 13 the PMMA master grating α before and after imprinting and the imprinted blazed grating α in OrmoCore on Si is shown. The parameters used to write this grating can be found in table 2. It can be seen that the master deforms slightly during imprinting, resulting in a different shape for the imprinted grating compared to the master. According to simulations, this grating has an incoupling efficiency of 35%. To further improve the efficiency the grating top should be smaller compared to the total width of the grating.

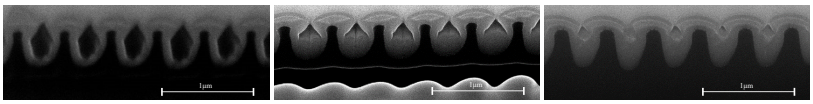

Fig. 13. FIB SEM cross section images of the PMMA master grating α on Si (a) before and (b) after imprinting and the (c) imprinted grating α in OrmoCore on Si.

In Fig. 14 two imprinted gratings β and γ in OrmoCore on Si with a higher incoupling efficiency are displayed together with their corresponding master in PMMA on Si after imprinting. The blazed grating β in Fig. 14(b) can achieve an incoupling efficiency of 45%, while the blazed grating γ in Fig. 14(d) can achieve 50%, so these second grating EBL parameters are used to write two larger blazed gratings to measure the diffraction efficiencies and to project an image on the real world scene. With these parameters it takes 7 min to write one writefield of 200x500 μm^2. Hence, a grating area of 2x3 mm^2 is chosen to have an acceptable e-beam writing time for fabricating two blazed gratings, 3 cm apart, on one master.

As discussed before, a blazed grating of several mm^2 consists of multiple writefields. So, the stitching errors in a 3x2 mm^2 blazed grating are also investigated with FIB SEM. In Fig. 15(a) and in Fig. 15(b) a horizontal and vertical stitching error can be seen in top- and cross sectional view, respectively. The line of dots is the horizontal stitching error in Fig. 15(a), at the vertical

Table 2. The EBL parameters corresponding to the gratings in Fig. 13 and 14

Grating	Fill factor	Doses [$\frac{\mu C}{cm^2}$]
Grating α in fig. 13	0.54	346-326-277
Grating β in fig. 14(a-b)	0.66	339-321-275
Grating γ in fig. 14(c-d)	0.66	321-303-248

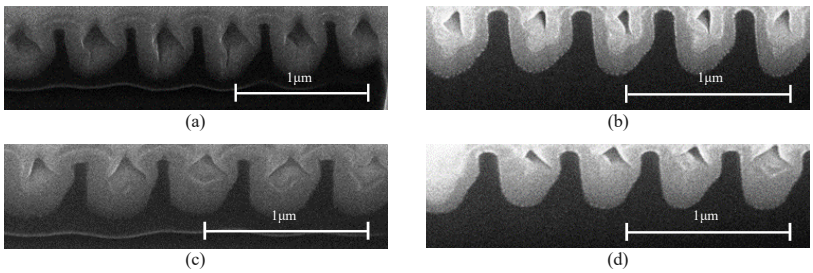

Fig. 14. FIB SEM cross section images of the two imprinted gratings β and γ in OrmoCore on Si and their PMMA master grating profiles on Si after imprinting. (a) Master grating β after imprinting. (b) Imprinted grating β. (c) Master grating γ after imprinting. (d) Imprinted grating γ.

stitching the dot is at a lower position. In Fig. 15(b), the middle structure is smaller compared to the others, this is the vertical stitching error. These errors can lead to dispersion of the incident laser spot or image.

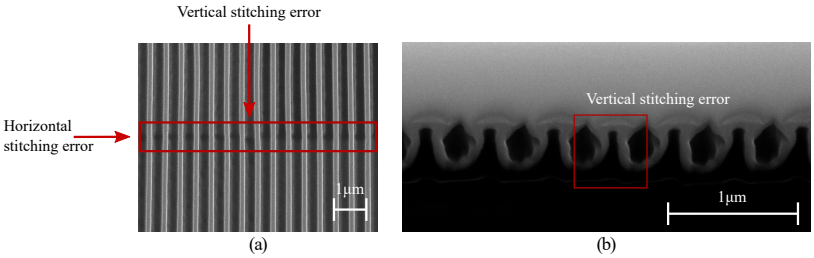

Fig. 15. FIB SEM images of the stitching errors between different writefields. (a) Horizontal and vertical stitching error in top view. (b) Vertical stitching error in cross sectional view.

Finally, two cross sections at two different places and a long cross section are made of the imprinted 3x2 mm^2 grating γ in OrmoCore on Si to check the variation in shape and pitch, this is shown in Fig. 16. A varying pitch can lead to distortion in the projected image, while a varying shape can lead to intensity differences. The pitch is 500 nm ± 10 nm. The height and fill factor change more over the grating area: H = 480 nm ± 40 nm and FF = 0.6 ± 0.07.

4.2. Optical measurements and demonstration

To quantify the diffraction efficiency, the master with two blazed gratings of 3x2 mm^2 is imprinted in OrmoCore on 5-mm-thick PMMA. As a reference, the master with the two binary gratings is imprinted in OrmoCore on 5-mm-thick PMMA as well. A picture of both the masters and the imprinted gratings can be found in Fig. 17. Their diffraction efficiencies are analyzed and

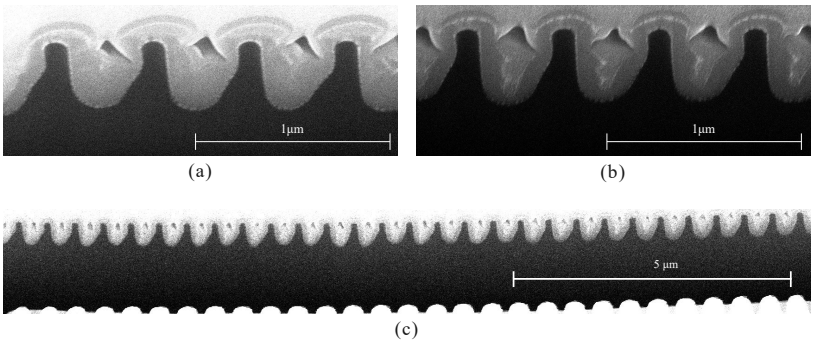

Fig. 16. FIB SEM images to evaluate the variation in pitch and shape over the total grating area of the blazed grating γ. (a-b) Two FIB SEM cross section images at two different places. (c) A long FIB SEM cross section image.

compared in two ways: by measuring the amount of light that is coupled in by one grating and by measuring the throughput of both gratings. Figure 18 shows the measurement setup: the grating is illuminated with linearly polarized green laser light (543.5 nm, Helium-Neon Laser 1652, JDS Uniphase, Milpitas, CA, USA) and the power is measured with a detector (Newport Model 818-SL) connected to a power meter (Newport 1930C optical power meter, Newport Corporation, Irvine, CA, USA). The TIR is visible in the PMMA sample on the picture of the setup in Fig. 18.

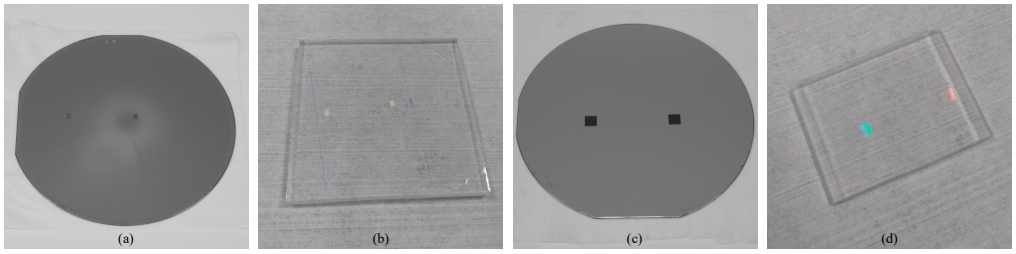

Fig. 17. The masters with (a) blazed and (c) binary gratings in PMMA on Si and the imprints of the (b) blazed and (d) binary gratings in OrmoCore on 5-mm-thick PMMA.

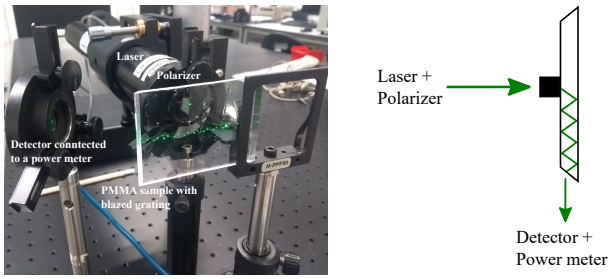

Fig. 18. A picture and a schematic of the optical setup for diffraction efficiency measurements.

For the first experiment, two 45° facets are polished at the PMMA waveguide sheet, as is schematically shown in Fig. 19. The green laser illuminates the grating perpendicularly and the power is measured at both facets and in the zeroth diffraction order for perpendicular as well as parallel polarized light. Simulations show that the highest efficiency for blazed gratings is

achieved when the light is polarized parallel to the grating lines and when it is diffracted in the direction where the slope is oriented to. This is confirmed with the measurements. For the blazed grating, 48.4% of the incident parallel polarized light is coupled out at the facet where the slope is oriented to, while 16.1% is coupled out at the other facet. 26.8% is recorded at the zeroth diffraction order. For a symmetric binary grating, 28.1% and 26.4% are coupled to the facets and 45.2% is transmitted to the zeroth diffraction order. For perpendicular polarized light the amount of light that is measured in the first diffraction orders is much lower, while the amount of light that is coupled to the zeroth diffraction order is increased a lot. The measured values can be found in table 3.

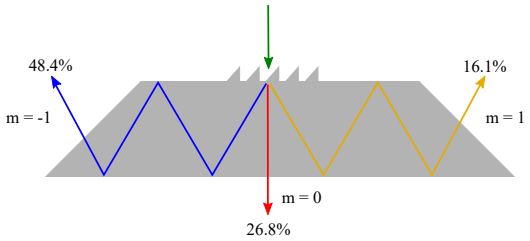

Fig. 19. The measured power at both 45° polished facets and in the zeroth order when the blazed grating is illuminated by parallel polarized green laser light.

Table 3. The measured diffraction efficiencies to the zeroth and first diffraction orders for a blazed and a binary grating for parallel and perpendicular polarized light.

Blazed grating	First order (m=-1)	Zero order (m=0)	First order (m=1)
Parallel	48.4%	26.8%	16.1%
Perpendicular	12.9%	79.0%	6.8%
Binary grating	First order (m=-1)	Zero order (m=0)	First order (m=1)
Parallel	28.1%	45.2%	26.4%
Perpendicular	2.58%	91.9%	3.23%

For the second experiment, green laser light illuminates the first grating perpendicularly and the light is coupled in the slab waveguide where it propagates due to TIR until it is coupled out by the second grating. The throughput is measured. This is the ratio between the intensity of the outcoupled light and the intensity of the light incident on the input grating. In Fig. 20 a throughput of 17.4% is measured for blazed gratings when parallel polarized light is following the green path in Fig. 20, while only 3.23% is measured when the light follows the red path. For binary gratings a throughput of 2.74% and 4.19% is measured. Next to the throughput in both directions, also the power of the light coupled to the zeroth diffraction order is measured. The elaborated results can be found in table 4.

A modified picoprojector (UO smart beam laser portable mini projector, SK Telecom, Seoul, South Korea) is used to demonstrate the HMD principle, see Fig. 21 for a picture and a schematic of the setup. For this demo, the lens in the picoprojector is replaced by a combination of 2 other lenses, i.e. a plano concave lens with a focal length of -50 mm and a plano convex lens with a focal length of 40 mm, to enhance the collimation of the light beam. The power coming out of the picoprojector is attenuated 1000 times. A 5x6 chess pattern of green and black squares is projected on the PMMA sample and perceived as a virtual image behind the waveguide. A white screen is used to obtain camera images which are easier to evaluate. The pictures can be found in

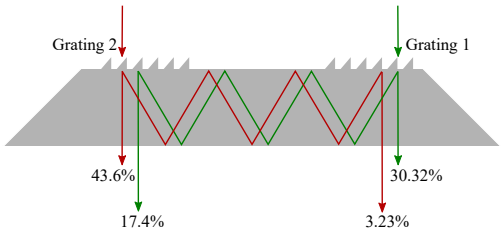

Fig. 20. The measured throughput and diffraction efficiencies to the zeroth diffraction order for two blazed gratings for parallel polarized green laser light.

Table 4. The measured throughput and diffraction efficiencies to the zeroth diffraction order for two blazed and two binary gratings for parallel and perpendicular polarized light.

Blazed gratings	Grating 1 to Grating 2	Zero order from Grating 1	Grating 2 to Grating 1	Zero order from Grating 2
Parallel	17.4%	30.32%	3.23%	43.6%
Perpendicular	1.81%	77.1%	0.32%	79.0%
Binary gratings	Grating 1 to Grating 2	Zero order from Grating 1	Grating 2 to Grating 1	Zero order from Grating 2
Parallel	2.74%	50.0%	4.19%	45.8%
Perpendicular	0.09%	91.6%	0.26%	89.7%

Fig. 22. The perceived AR image, coupled in- and out by blazed gratings in Fig. 22(b), appears clear and sharp and the stitching errors are not visible in the pattern. The fact that the image is quite small and not sharp at the edges is a result of the limited grating area and can be improved by writing larger gratings. The image projected by the 5x5 mm^2 binary gratings in Fig. 22(a) is less bright and less sharp. Finally, a picture is taken of the chess pattern superimposed on the real world scene by using the blazed gratings, see Fig. 22(c). The image appears in focus at 4 m in front of the waveguide. This distance can be tuned by varying the distance between the two lenses in front of the picoprojector. By using these efficient blazed grating structures the required power levels for the HMD can be limited.

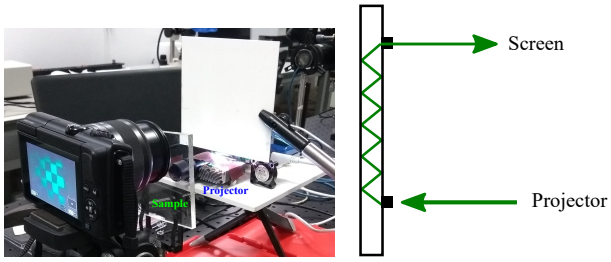

Fig. 21. A picture and a schematic of the setup for the demonstration of a waveguide-type HMD.

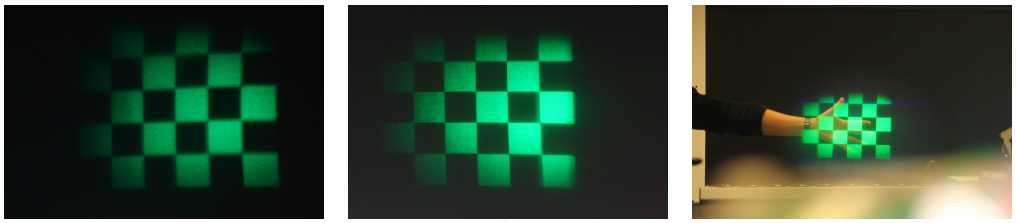

(a) (b) (c)

Fig. 22. (a) The chess pattern projected by binary gratings on a screen. (b) The chess pattern projected by blazed grating on a screen. (c) The chess pattern projected by blazed gratings on the environment.

5. Conclusion

In this paper we demonstrated a waveguide-type HMD with blazed gratings, which are 4 times more efficient than binary gratings. First, three types of asymmetric 3D gratings were investigated in Lumerical. Each grating profile was designed to achieve an in- and outcoupling efficiency of 55% or higher. EBL was used to fabricate these structures by modulating the electron-dose over the grating pitch. After several optimization cycles, a grating profile was achieved that, theoretically, could achieve an incoupling efficiency of 50%. Two of such gratings were fabricated, 3 cm apart, on one master with EBL and afterwards imprinted with UV-NIL on a waveguide sheet. These blazed gratings proved to be very efficient: an incoupling efficiency of 48.4% and a throughput efficiency of 17.4% were recorded. Finally, it could be shown that an image injected in the waveguide and extracted in front of the eye appeared sharp and non-distorted superimposed on the real world scene. By using these efficient blazed grating structures the required power levels for the HMD can be limited.

Funding

This research was funded within the imec.icon project smartGLAZ, bringing academia and industry together (Flanders Innovation Entrepreneurship project nr. HBC.2017.0634).

Acknowledgments

We want to thank Regan Watts and Jochen Vleugels from the University of Antwerp for providing us with the picoprojector. We also want to thank Lothar Mader from IMEC for polishing the PMMA samples.

Disclosures

The authors declare no conflicts of interest.

References

1. V. Brac de la Perrière, "Understanding waveguide-based architecture and ways to robust monolithic optical combiner for smart glasses," Proc. SPIE 10676, 106761D (2018).
2. C. Pan, Z. Liu, Y. Pang, X. Zheng, H. Cai, Y. Zhang and Z. Huang, "Design of a high-performance in-coupling grating using differential evolution algorithm for waveguide display," Opt. Express **26**(20), 26646-26662 (2018).
3. M.-L. Piao, S.-K. Gil and N. Kim, "Design of wide angle holographic waveguide monocular head-mounted display using photopolymer," Proc. SPIE 9386, 93860K (2015).
4. J. Guo, Y. Tu, L. Yang, L. Wang and B. Wang, "Holographic waveguide display with a combined-grating in-coupler," Appl. Opt. **55**(32), 9293-9298 (2016).
5. M.-U. Erdenebat, Y.-T. Lim, K.-C. Kwon, N. Darkhanbaatar and N. Kim, "State of the Art Virtual Reality and Augmented Reality Knowhow - Waveguide-Type Head-Mounted Display System for AR Application," (IntechOpen, 2018) Chap. 4.

6. M. W. Farn, "Binary gratings with increased efficiency,"Appl. Opt. **31**(22), (1992).
7. F. Van Laere, M.V. Kotlyar, D. Taillaert, D. Van Thourhout, T.F. Krauss and R. Baets, "Compact Slanted Grating Couplers Between Optical Fiber and InP-InGaAsP Waveguides," IEEE Photonics Technol. Lett. **19**(6), 396-398 (2007).
8. J. Schrauwen, F. Van Laere, D. Van Thourhout and R. Baets, "Focused-Ion-Beam Fabrication of Slanted Grating Couplers in Slicon-on-Insulator Waveguides," IEEE Photonics Technol. Lett. **19**(11), 816-818 (2007).
9. T. Levola and P. Laakkonen, "Replicated slanted gratings with a high refractive index material for in and outcoupling of light," Opt. Express **15**(5), 2067-2074 (2007).
10. B. Zhang, Q. Wang, N. Shen and H. Ding, "Experimental Investigation and Numerical Analysis of Mechanical Ruling for an Aluminum-Coated Diffraction Grating," J. Manuf. Sci. Eng. **139**, (2017).
11. J. Shi, B. Sheng, Y.-S. Huang, L.-N. Peng, L.-Y. Wang, Z.-J. Ni, D.-W. Zhang, Y.-F. Zhao and M. He, "Multifacet echelle grating for intensity broadening on spectral plane fabricated by rotating ion-beam etching,"Appl. Opt. **58**(18), 5040-5044 (2019).
12. D. L. Voronov, M. Ahn, E. H. Anderson, R. Cambie, C.-H. Chang, E. M. Gullikson, R. K. Heilmann, F. Salmassi, M. L. Schattenburg, T. Warwick, V. V. Yashchuk, L. Zipp and H. A. Padmore, "High-efficiency 5000 lines/mm multilayer-coated blazed grating for extreme ultraviolet wavelengths,"Opt. Lett. **35**(15), 2615-2617 (2010).
13. A. Schleunitz, V.A. Guzenko, M. Messerschmidt, H. Atasoy, R. Kirchner and H. Schift, "Novel 3D micro- and nanofabrication method using thermally activated selective topography equilibration (TASTE) of polymers," Nano Converg. **1**, 7 (2014).
14. A. Schleunitz and H. Schift, "Fabrication of 3D nanoimprint stamps with continuous reliefs using dose-modulated electron beam lithography and thermal reflow," J. Micromech. Mircoeng. **20**(9), 095002 (2010).
15. R. Kirchner, V.A. Guzenko, I. Vartiainen, N. Chidambaram and H. Schift, "ZEP520A - A resist for electron-beam grayscale lithograpy and thermal reflow," Microelectron. Eng. **153**, 71-76 (2016).
16. T. Shiono, T. Hamamoto and K. Takahara, "High-efficiency blazed diffractive optical elements for the violet wavelength fabricated by electron-beam lithography," Appl. Opt. **41**(13), 2390-2393 (2002).
17. J. Missinne, N. Teigell Benéitez, M.-A. Mattelin, A. Lamberti, G. Luyckx, W. Van Paepegem and G. Van Steenberge, "Bragg-Grating-Based Photonic Strain and Temperature Sensor Foils Realized Using Imprinting and Operating at Very Near Infrared Wavelengths," Sensors **18**(8), 2717 (2018).
18. J. Missinne, N. Teigell Benéitez, A. Lamberti, G. Chiesura, G. Luyckx, M.-A. Mattelin, W. Van Paepegem and G. Van Steenberge, "Thin and flexible polymer photonic sensor foils for monitoring composite structures," Adv. Eng. Mater. **20**(2), 1701127 (2018).
19. K. Mohamed, M.M. Alkaisi and R.J. Blaikie, "A Three-Dimensional Ultraviolet Curable Nanoimprint Lithography (3D UV-NIL)," AIP Conf. Proc. 1151, 114 (2009).
20. N. Kooy, K. Mohamed, L.T. Pin and O.S. Guan, "A review of roll-to-roll nanoimprint lithography," Nanoscale Res. Lett. **9**, 320 (2014).
21. S.H. Ahn and L.J. Guo, "Large-Area Roll-to-Roll and Roll-to-Plate Nanoimprint Lithography: A Step toward High-Throughput Application of Continuous Nanoimprinting," ACS Nano **3**(8), 2304-2310 (2009).
22. NDT Resource Center, "The Human's Eye Response to Light," https://www.nde-ed.org/EducationResources/CommunityCollege/PenetrantTest/Introduction/lightresponse.htm.
23. A.S. Gangnaik, Y.M. Georgiev and J.D. Holmes, "New Generation Electron Beam Resists: A Review," Chem. Mater. **29**(5), 1898-1917 (2017).
24. E. Herth, E. Algre, P. Tilmant, M. Francois, C. Boyaval and B. Legrand, "Performances of the Negative Tone Resist AZnLOF 2020 for Nanotechnology Applications," IEEE Trans. on Nanotechnol. **11**(4), 854-859 (2012).